

Experimental and analytical studies on shear behaviors of FRP-concrete composite sections

Zou, Xingxing; Feng, Peng ; Bao, Yi; Wang, Jingquan ; Xin, Haohui

DOI

[10.1016/j.engstruct.2020.110649](https://doi.org/10.1016/j.engstruct.2020.110649)

Publication date

2020

Document Version

Accepted author manuscript

Published in

Engineering Structures

Citation (APA)

Zou, X., Feng, P., Bao, Y., Wang, J., & Xin, H. (2020). Experimental and analytical studies on shear behaviors of FRP-concrete composite sections. *Engineering Structures*, 215, Article 110649. <https://doi.org/10.1016/j.engstruct.2020.110649>

Important note

To cite this publication, please use the final published version (if applicable). Please check the document version above.

Copyright

Other than for strictly personal use, it is not permitted to download, forward or distribute the text or part of it, without the consent of the author(s) and/or copyright holder(s), unless the work is under an open content license such as Creative Commons.

Takedown policy

Please contact us and provide details if you believe this document breaches copyrights. We will remove access to the work immediately and investigate your claim.

1 **Experimental and analytical studies on shear behaviors of FRP-concrete composite sections**

2 Xingxing Zou¹, Peng Feng², Yi Bao³, Jingquan Wang^{4*} and Haohui Xin⁵

3 ¹ Department of Civil, Architectural & Environmental Engineering, Missouri Univ. of Science and
4 Technology, Rolla, MO 65409. E-mail: zxbn4@mst.edu

5 ² Department of Civil Engineering, Tsinghua University, Beijing 100084, China; E-mail:
6 fengpeng@tsinghua.edu.cn

7 ³ Department of Civil, Environmental and Ocean Engineering, Stevens Institute of Technology,
8 Hoboken, NJ 07030. E-mail: yi.bao@stevens.edu

9 ⁴ Key Laboratory of Concrete and Prestressed Concrete Structures of the Ministry of Education,
10 Southeast University, Nanjing 210096, China. E-mail: wangjingquan@seu.edu.cn (corresponding
11 author)

12 ⁵ Faculty of Civil Engineering and Geosciences, Delft University of Technology, Delft, the
13 Netherlands, E-mail: h.xin@tudelft.nl

14

15 **ABSTRACT**

16 The design of FRP profile-concrete composite sections, including beams and decks, is usually
17 governed by the shear strength of the FRP profiles. However, analytical methods that can precisely
18 predict the shear capacity of the composite sections have not been well developed, because there
19 is lack of knowledge of the FRP-concrete composite action and distribution of shear stress along
20 the FRP. This paper investigates the shear behaviors of FRP-concrete composite sections and
21 develops formulae to predict the shear capacity of the composite sections. First, flexural tests of
22 three FRP-concrete composite beams were conducted to investigate the shear failure mode and
23 interface behaviors. All the beams failed in FRP shear fracture along horizontal direction. Then,
24 push-out tests were used to determine the slip property for the FRP-concrete interface which
25 reveals that FRP stay-in-place form and steel bolts can ensure full and partial composite action,
26 respectively. Based on the experimental study, closed-form equations to compute the maximum
27 shear stress are derived and validated against experimental data in this paper and literature. Finally,
28 simple yet reliable equations of shear capacity are derived and recommended for engineers to
29 design the FRP-concrete composite sections.

30

31 **Key words:** shear capacity; FRP-concrete composite sections; composite action; slip effect; shear
32 connection.

33 **Notation**

A_{web}	=	cross sectional area of FRP web(s);
A_C, A_F	=	cross sectional area of concrete and FRP, respectively;
$A_F(y)$	=	parameter in equations;
b	=	shear span length of beam specimens;
b_C, b_F	=	width of concrete slab and FRP flange, respectively;
E_C, E_{Fx}	=	elastic modulus of concrete and FRP (in longitudinal direction), respectively;
h_0	=	distance between the neutral axis of concrete and FRP;
h_C, h_F	=	height of concrete and FRP, respectively;
I_C, I_F	=	moment inertia of concrete and FRP, respectively;
k	=	smear slip modulus of the interface;
K	=	slip modulus per connector;
L	=	beam span;
$m(x)$	=	ratio given by $m(x) = h_0 k s(x) / V(x)$;
m_0	=	value of $m(x)$ at the support points of beams;
m_{full}	=	value of m_0 with full composite action;
$M_C(x), M_F(x)$	=	flexural moment carried by concrete and FRP, respectively;
n	=	number of rows of the connector in lateral direction;
n_0	=	number of studs in one push-out test specimens;
$N_C(x), N_F(x)$	=	axial force in concrete and FRP, respectively;
p	=	longitudinal space between two adjacent connectors;
P	=	total applied load;
P_u	=	experimental ultimate load;
$r(x)$	=	distributed normal force along FRP and concrete interface;
$s(x)$	=	interfacial slip;
s_0	=	slip at the load of $0.5P_u$ of push-out test;
s_{max}	=	maximum slip;
S_{xy}	=	shear strength of FRP web(s);
$S_F(y), S_C(y)$	=	parameters in equations;
$t(y)$	=	thickness of FRP web or FRP width;

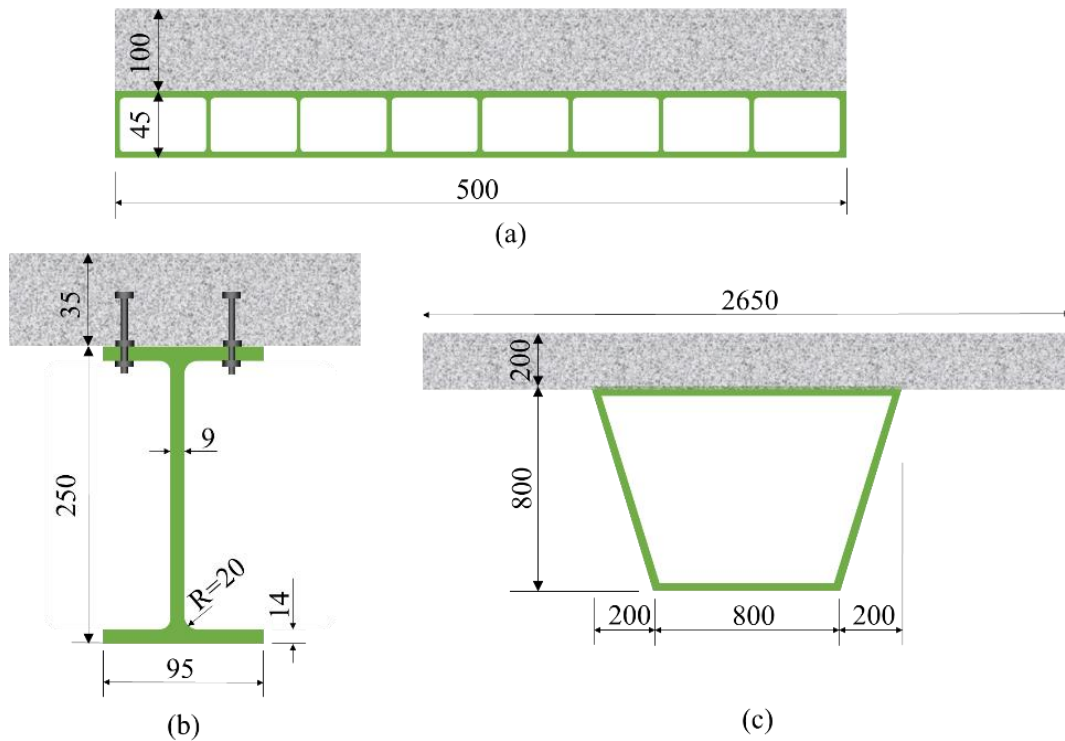
- t_{web} = thickness of FRP web;
 V_1, V_2 = shear capacity computed by Eq. (1) and Eq. (2), respectively;
 $V(x), V_C(x), V_F(x)$ = shear force carried by the composite section, concrete and FRP, respectively;
 V_{test} = experimental shear capacity of beam specimens;
 X_C = compressive strength of FRP;
 y_0 = vertical coordinate of the location of maximum shear stress;
 $y_{0,ana}$ = analytical value of y_0 ;
 $y_{0,test}$ = experimental value of y_0 ;
 $\alpha, \beta, A_0, A_1, I_0$ = parameters used to simplify the equations;
 α_E = ratio of E_{Fx} over E_C ;
 α_1 = ratio of cross sectional area of FRP flanges over concrete;
 α_2 = ratio of h_F and h_C ;
 δ_u = maximum mid-span deflection;
 $\varepsilon_C(x, y), \varepsilon_F(x, y)$ = strains of concrete and FRP, respectively;
 $\varepsilon_{slip}(x)$ = strain difference caused by the slip at FRP-concrete interface;
 η_C, η_F = contribution ratio of concrete and FRP, respectively;
 η_{SD} = ratio of maximum shear stress over average shear stress;
 $v(x)$ = distributed interfacial shear force along longitudinal direction;
 $\sigma_F(x, y)$ = normal stress of FRP;
 $\tau_C(x, y), \tau_F(x, y)$ = shear stress of concrete and FRP, respectively;
 τ_{max} = maximum shear stress;
 ϕ = curvature of the beam.

35 1. Introduction

36 Fiber reinforced polymer (FRP) has extraordinary mechanical and in-service properties, which can
37 improve the stiffness, strength, durability, life-cycle cost, and environmental impacts when combined with
38 other construction materials [1]. Recently, there are increasing research interests and filed applications of
39 FRP profiles-concrete composite (or hybrid) structures, particularly in the forms of bridge decks [2], girders
40 [3][4], and floor systems [5][6]. The FRP-concrete systems maximize the advantages of the materials by
41 integrating FRP that is extremely durable and lightweight with concrete that is low-cost and has desired
42 compressive strength [7][8]. Among various FRP-concrete systems, FRP-concrete composite beams/decks
43 (see Fig. 1) demonstrated superior cost-effectiveness and high durability, compared with traditional steel-
44 concrete composite structures and all-FRP structures [1][3][4][9][10][11]. Hereafter, FRP-concrete
45 composite (or hybrid) beam/deck is referred as FRP-concrete composite section for a general meaning. The
46 concrete slab is cast on top of an FRP profile (see Fig. 1). The concrete and FRP are joined by interfacial
47 shear connection such as epoxy adhesives [5], perforated FRP ribs [2][9], steel bolts [3][11], FRP bolts [3],
48 or FRP shear keys [4][8]. Flexural tests showed that glass FRP (GFRP)-concrete composite beams had
49 higher stiffness and strength, compared with all GFRP profiles [12]. On the other side, compared to the
50 equivalent reinforced concrete (RC) beams, the hybrid GFRP-concrete specimens displayed approximate
51 50% higher ultimate capacity with 50% less weight [12].

52 Pultrusion is a cost-effective and efficient technique to manufacture FRP profiles with high quality
53 control [1]. Pultruded FRP profiles have been widely used in FRP-concrete composite sections [13][14][15].
54 Although FRP-concrete composite sections follow the same concept as steel-concrete composite sections,
55 a salient difference is that the shear strength of pultruded FRP is fairly lower than that of steel profiles (see
56 Table 1) [16][17][18][19]. Owing to the low shear strength, flexural tests on FRP-concrete composite
57 sections often induce undesirable and catastrophic shear failure at FRP web or web-top flange junction at
58 relatively low load levels [8][12][20][21]. Both GFRP-concrete interface failure and shear failure in GFRP
59 webs have been observed from existing tests [20]. The GFRP-concrete bond failure can be avoided by
60 developing effective shear connectors [8][9][22][23][24]. Therefore, the shear capacity usually governs the

61 design of the FRP-concrete composite sections, which means precisely computing the shear capacity plays
 62 a critical role in the design.



63
 64 **Fig. 1.** Typical cross section of: (a) FRP-concrete hybrid deck [2]; (b) open-section FRP-concrete hybrid
 65 beam [3]; and (c) closed-section FRP-concrete hybrid beam [4]. Unit in mm.

66 **Table 1.** Typical ratio of shear strength (S_{xy}) and compression strength (X_c) of FRP and steel

Profile	Company	S_{xy} (MPa)	X_c (MPa)	S_{xy}/X_c
GFRP	Fiberline [16]	31	240	1/8
GFRP	Strongwell [17]	31	207	1/7
GFRP	Topglass [18]	25	220-230	1/12~1/9
GFRP	Creative Pultrution [19]	23-31	227-316	1/14~1/7
Steel		135	235 (Yield)	1/1.7

67
 68 Currently, all the existing methods for the shear capacity of FRP-concrete composite sections neglect
 69 the shear resistance of the concrete slab [20][21]. It is reasonable to neglect the shear resistance of the
 70 concrete slab in steel-concrete composite beams, because the shear strength of the steel beam is typically
 71 much higher than that of the concrete. However, since the shear strength of FRP profile is typically low,
 72 neglecting the shear resistance of concrete may significantly compromise the accuracy of the analysis. For

73 example, it was assumed in [21] that the shear force was carried only by the FRP webs, and the shear stress
 74 was uniform along the height of the FRP webs. Accordingly, the shear capacity of FRP-concrete composite
 75 sections was expressed as:

$$V_1 = A_{web}S_{xy} \quad (1)$$

76 where V_1 is the shear capacity; A_{web} is the total cross sectional area of the FRP web(s); S_{xy} is the shear
 77 strength of the FRP web(s). However, the assumption of the uniform shear stress distribution is not
 78 consistent with the reality. Hence, it was assumed in [20] that the maximum shear stress in FRP webs was
 79 1.5 times the average shear stress. So, the shear capacity was expressed as:

$$V_2 = \frac{2}{3}A_{web}S_{xy} \quad (2)$$

80 where V_2 is the shear capacity. Table 2 shows the test results of 12 specimens with a shear failure at FRP
 81 web(s) or top-flange-web joints [5][8][12][21]. Eqs. (1) and (2) underestimated the shear capacity by 18%
 82 and 45%, respectively. There is a need to develop a more accurate method to predict the shear capacity of
 83 the FRP-concrete composite sections.

84 **Table 2.** Comparison between analytical [Eqs. (1) and (2)] and experimental results of shear capacity

Reference	Specimen	Profile depth (mm)	Web thickness (mm)	Web area (mm ²)	S_{xy} (MPa)	V_1 (kN)	V_2 (kN)	V_{test}^*a (kN)	$\frac{V_1}{V_{test}}$	$\frac{V_2}{V_{test}}$
[8]	HB	150	10	1500	25.3	37.5	25.0	49.6	0.76	0.50
	HB-T	150	10	1500	25.3	37.5	25.0	74.8	0.50	0.33
	HB-R	150	10	1500	25.3	37.5	25.0	47.3	0.79	0.53
[21]	Beam C*-S	228.6	11.1×2	5075	31.0	157.3	104.9	170.5	0.92	0.62
	Beam S*-S	228.6	11.1×2	5075	31.0	157.3	104.9	191.5	0.82	0.55
[5]	HB1	200	10	2000	47.1 ^{*b}	94.2	62.8	91.00	1.04	0.69
	HB3	200	10	2000	47.1 ^{*b}	94.2	62.8	148.10	0.64	0.42
	HB5	200	10	2000	47.1 ^{*b}	94.2	62.8	87.90	1.07	0.71
[12]	M2-HB1	120	8	960	35.0	33.6	22.4	39.00	0.86	0.57
	M2-HB2	120	8	960	35.0	33.6	22.4	37.67	0.89	0.59
	M2-HB3	120	8	960	35.0	33.6	22.4	44.88	0.75	0.50
	M2-HB4	120	8	960	35.0	33.6	22.4	45.63	0.74	0.49
Average									0.82	0.55

85 *a. V_{test} is the test result of the shear capacity of the specimens.

86 *b. The value was provided by the authors of [12].

87 This paper investigates the shear behavior of FRP-concrete composite sections and develops formulae
 88 to accurately predict the shear capacity of the composite sections, aiming to advance the fundamental

89 understandings of the composite behaviors and provide effective tools for the design and evaluation of FRP-
90 concrete composite sections.

91

92 **2. Method**

93 This study aims at more advanced understanding of the shear behavior of FRP-concrete hybrid sections
94 and proposing a design method for the shear capacity considering the contribution of concrete.
95 Experimental tests were conducted in four-point bending, where the specimens were designed to be failed
96 in shear. An analytical approach, returned to the fundamental analysis of composite action, was proposed
97 to compute the shear stress of the specimen. The results of maximum shear stress given by derived equations
98 were compared against the experimental results. Based on the experimental study and the analytical
99 approach, closed-form equations of the shear capacity of the composite sections were derived, considering
100 the contribution of concrete and interfacial slip. Finally, methods and equations that can be conveniently
101 applied to design the FRP-concrete composite sections were explored.

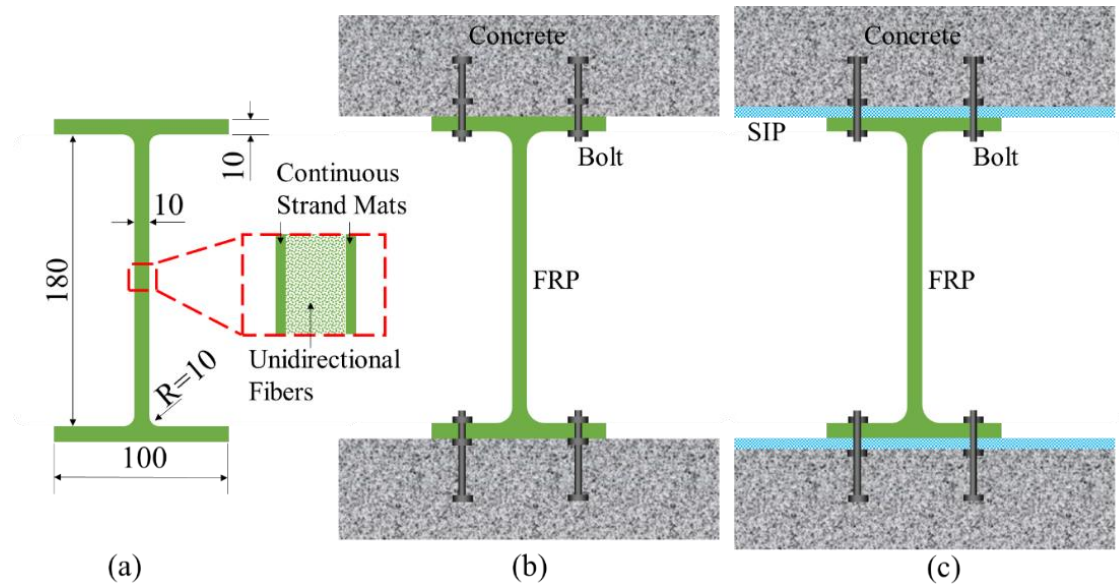
102

103 **3. Experimental Investigation**

104 This section presents the flexural test of FRP-concrete composite beams and push-out test of FRP-
105 concrete connectors. Subsection 2.1 introduces the materials and properties. Subsection 2.2 introduces the
106 flexural test. Subsection 2.3 introduces the push-out test.

107 **3.1. Materials**

108 FRP profiles (see Fig. 2a) were made from unsaturated polyester resin reinforced by glass fibers
109 through pultrusion technique. The FRP products are commercially available at the Nanjing Kangte
110 Composite Material Co., Ltd., in Nanjing, China [25]. The fiber layout of the FRP profiles is unidirectional
111 roving in the core sandwiched between two layers of continuous-strand mats along the outer surfaces (see
112 Fig. 2a). The mass percentage of fibers is approximate 45%, the mass percentage of resin is 35%, and the
113 left is CaCO₃ powder filler, according to the manufacturer.



114 (a) (b) (c)

115 **Fig. 2.** Cross sections of: (a) FRP profile, (b) push-out test specimens of Group I &II, and (c) push-out test
 116 specimens of Group III. SIP stands for stay-in-place formwork.

117 The density of the profiles is 1,900 kg/m³, as specified by the manufacturer. The tensile, compressive,
 118 and shear properties were obtained through testing tensile, compressive, and short three-point bending
 119 coupons, respectively, according to Chinese standard GB 50608–2010 [26]. The coupons were cut from the
 120 actual pultruded profiles and machined to the exact dimensions. The longitudinal tensile and compressive
 121 strengths were 420 MPa and 350 MPa, respectively. The longitudinal tensile and compressive moduli were
 122 25 GPa and 23 GPa, respectively. The shear strength was 9.2 MPa, which is lower than other commercial
 123 products shown in Table 1. The low shear strength is attributed to the lack of multi-directional fibers on the
 124 webs and the use of CaCO₃ powder as the filler in the resin matrix.

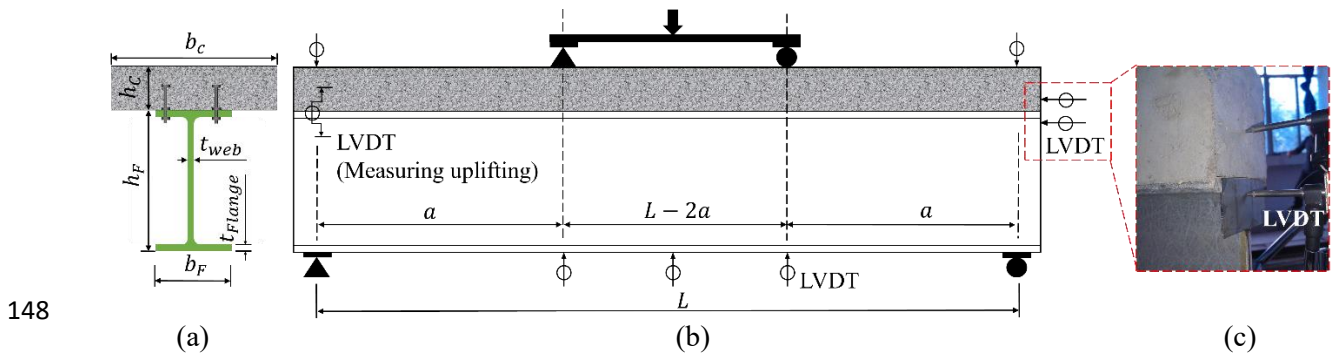
125 The concrete was designed to achieve a compressive strength of 30 MPa at 28 days. The specimens
 126 were cast and tested in accordance with Chinese standard GB 50010–2010 [27]. The average values of the
 127 elastic modulus, compressive strength, and compressive strain at peak stress of the concrete were 28.2 GPa,
 128 29.5 MPa, and 0.00263, respectively. All push-out and flexural specimens were cured under identical
 129 condition as the coupons for material properties testing.

130 Steel bolts (see Figs. 2b and 2c) were fixed on the top flanges of the FRP profiles using nuts and
 131 washers on both sides of the FRP flange plate. The steel bolts serve as headed studs that integrate the

132 concrete and FRP. The grade of the steel was Grade M10 8.8 with the tensile and yield strengths of 800
 133 MPa and 640 MPa, respectively. For the meaning of the Grade $Ma\ b.c$, the diameter of the stud shank is a
 134 mm, the tensile strength is $b \times 100$ MPa, and the ratio of yield strength over tensile strength is $c \times 0.1$. The
 135 steel stud in this study had a diameter of 100 mm. The embedded length in concrete, defined as the distance
 136 from the top of the stud to the top of the FRP flange, was 80 mm. Steel washers, with an outer diameter of
 137 20 mm, inner diameter of 10.5 mm (slightly larger than the diameter of the studs) and a thickness of 2 mm,
 138 were used to distribute the local stress caused by axial pre-tightening force of the studs.

139 **3.2. Flexural test of FRP-concrete composite beams**

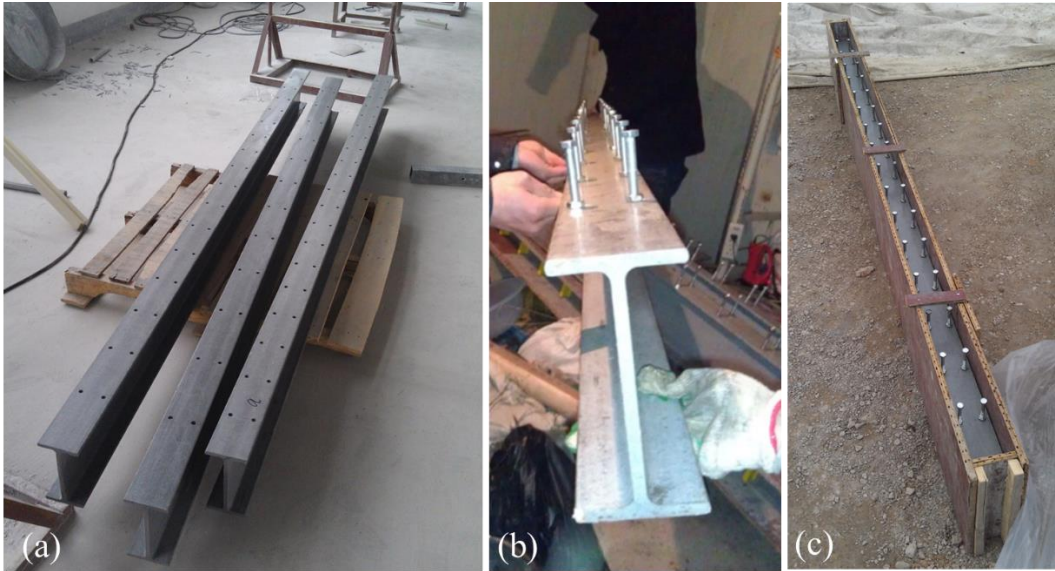
140 Three FRP-concrete composite beams were tested, as shown in Fig. 3. Each beam was composed of
 141 an I-shaped pultruded GFRP beam (see Fig. 2a, Fig. 3a) and a concrete slab (see Fig. 3). All specimens
 142 were simply supported and loaded under four-point bending. The deflections and the slippages were
 143 measured by linear variable differential transformers (LVDTs). The strains in FRP and concrete were
 144 measured by strain gauges. Two LVDTs were used to measure the horizontal displacements of FRP and
 145 concrete, respectively, and the different horizontal displacements indicated the interfacial slip. The web
 146 thickness (t_{web}) and flange thickness (t_{Flange}) of the FRP profile were 10 mm. The transversal space of
 147 the steel studs was 55 mm.



149 **Fig. 3.** FRP-concrete composite beam: (a) cross section, (b) side view, and (c) deployment of the LVDTs
 150 measuring slip.

151 The specimens were fabricated in four steps: (i) drill holes in the upper flanges of FRP profiles (see
 152 Fig. 4a), (ii) install steel studs at the predefined locations (see Fig. 4b), (iii) fabricate the wood formwork

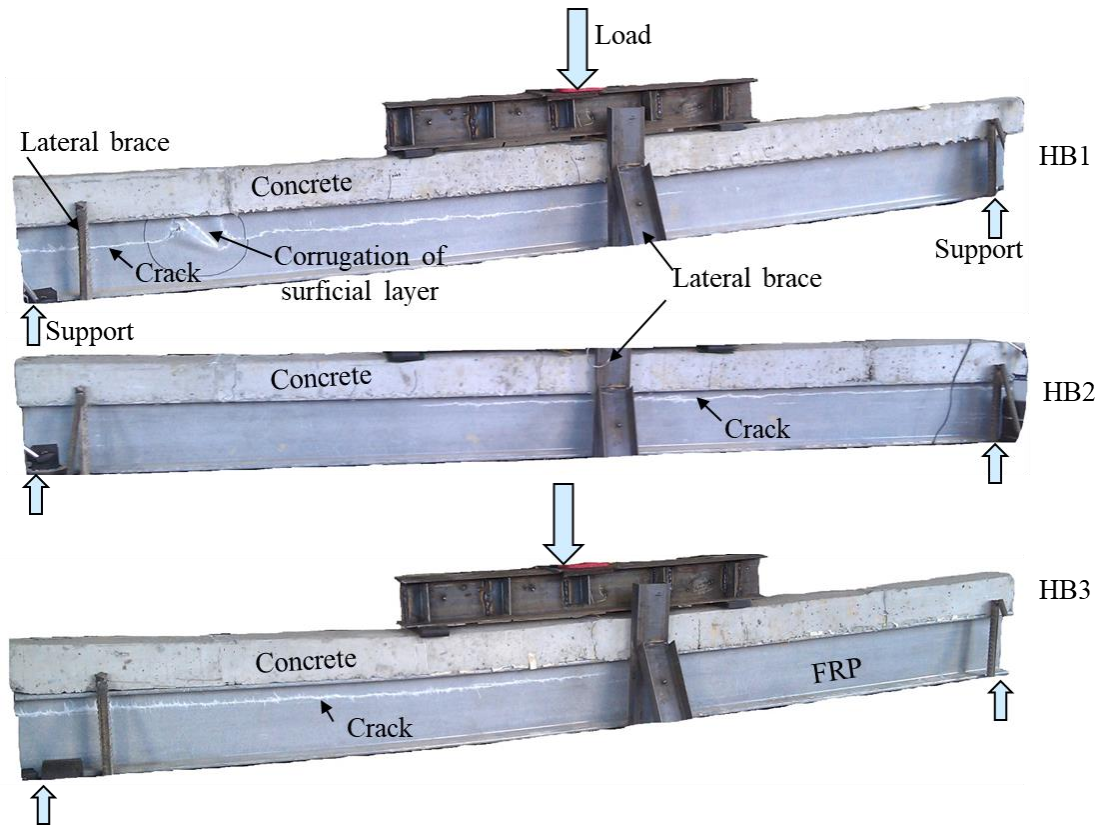
153 (see Fig. 4c), and (iv) cast concrete slab.



154

155 **Fig. 4.** Construction of FRP-concrete composite beam specimens: (a) FRP beams with drilled holes, (b) an
156 FRP beam with steel studs, and (c) wood forms.

157 Similar failure processes and modes were observed from the three specimens. Before the failure, there
158 was no notable acoustic activities and visible cracks. As the load reached the ultimate capacity, a crack on
159 FRP web occurred from the support and suddenly propagated to the mid-span in a few seconds (see Fig. 5),
160 resulting in a catastrophic and brittle failure.



161

162 **Fig. 5.** Failure modes of the FRP-concrete composite beam specimens tested under four-point bending.

163 The results are summarized in Table 3, where P_u is the experimental ultimate load, $y_{0,test}$ is the
 164 average vertical coordinate (the coordinate system will be introduced in the next section) of the main crack
 165 (see white lines in Fig. 5), $y_{0,ana}$ is the value which will be introduced in next section, δ_u is the maximum
 166 mid-span deflection, and s_{max} is the maximum slip.

167

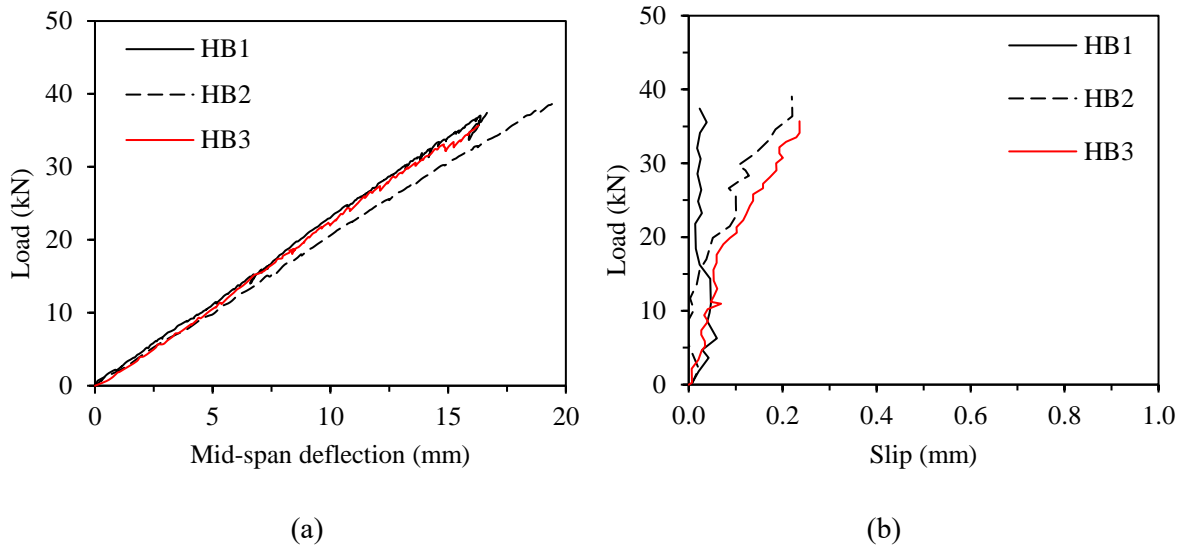
Table 3. Results of flexural tests

Specimen	h_c (mm)	b_c (mm)	P_u (kN)	$y_{0,test}$ (mm)	$y_{0,ana}$ (mm)	$\frac{y_{0,ana}}{y_{0,test}}$	δ_u (mm)	s_{max} (mm)
HB1	100	100	37.4	-56.5	-49.28	0.87	16.7	0.060
HB2	100	100	39.0	-61.5	-55.78	0.91	17.7	0.219
HB3	100	100	35.7	-58.6	-61.48	1.05	16.3	0.236

168

169 The load-deflection curves are plotted in Fig. 6a. The load increases approximately linearly with the
 170 mid-span deflection until the brittle shear failure. The load-slip relationships are plotted in Fig. 6b. The slip
 171 of HB1 was less than 0.06 mm, smaller than the rest two specimens, because HB1 had more steel studs as
 172 the shear connection. The slips of HB2 and HB3 were close, with a maximum value of 0.219 mm and 0.236

173 mm, respectively. The interfacial uplifting - vertical separation, measured by the vertical LVDT at the left
 174 side of the beam in Fig. 3b - was almost zero for all the beams during the loading.



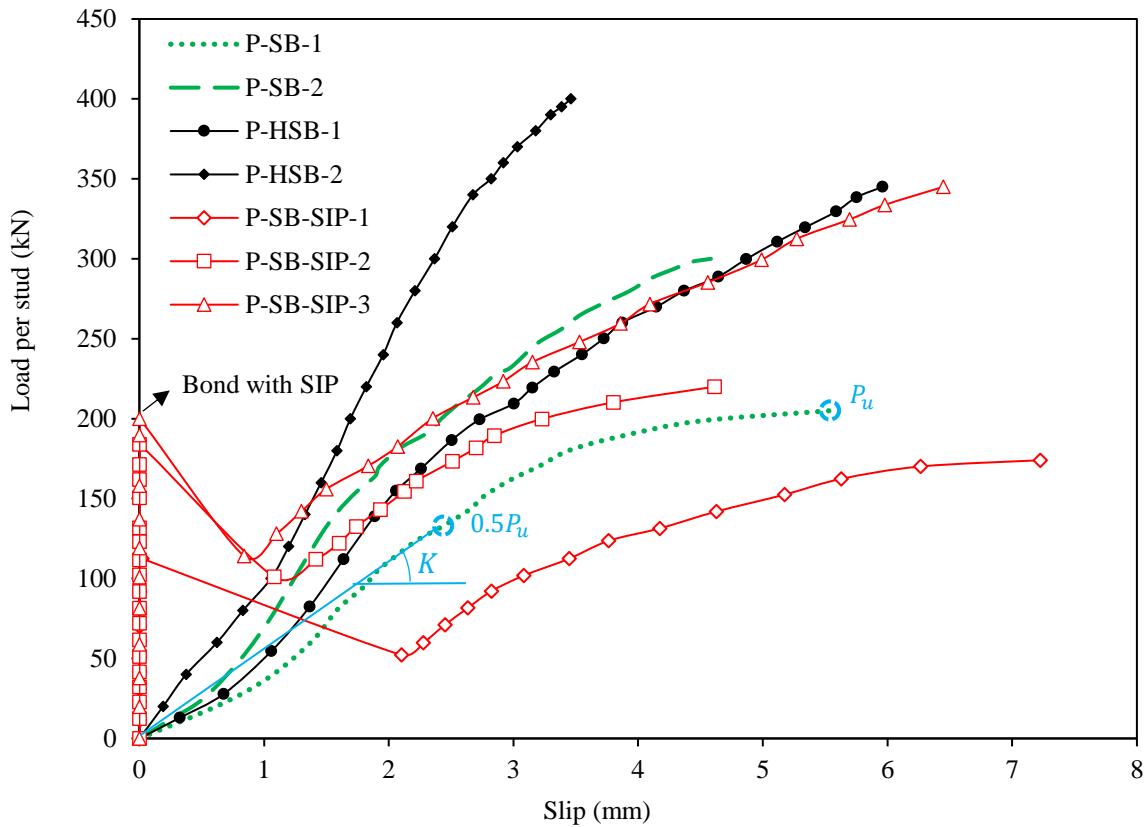
175
 176 (a) (b)
 177 **Fig. 6.** Test results of FRP-concrete composite beam specimens: (a) load-deflection responses, and (b) load-
 178 slip responses.

179 **3.3. Determining slip modulus from the load-slip response of push-out specimens**

180 In order to consider the slip between FRP and concrete, the slip stiffness for each connector, K , was
 181 experimentally determined through push-out tests (see Figs. 2b and 2c), as reported in [8]. Three groups of
 182 connectors were tested, namely Groups I, II, and III. Group I had ordinary steel studs (SB), Group II had
 183 high steel studs (HSB, the same as the studs used in beam test of this paper, see Section 2.2), and Group III
 184 used stay-in-place formwork (see Fig. 2c) between the FRP and concrete. The formwork provided bond
 185 with the concrete slab and eased the construction of concrete. Groups I and II showed two failure modes,
 186 namely the studs shank shear fracture and shear-out failure of FRP flange, as elaborated in [24]. Fig. 7 plots
 187 the load-slip response, which is a pivotal factor to evaluate the composite action of the FRP-concrete
 188 composite sections. The secant slope at half of the ultimate load, $0.5P_u$, is defined as slip modulus – K (see
 189 Fig. 7), which is given as:

$$K = \frac{0.5P_u}{n_0s_0} \quad (3)$$

190 where n_0 is the number of studs in a push-out test; s_0 is the slip at the load $0.5P_u$. Table 4 lists the results
 191 of K of push-out specimens in [5][8][24].



192
 193 **Fig. 7.** The relationship between the load per stud and interfacial slip between FRP and concrete. The bond
 194 between the SIP and concrete caused a zero-slip phase at the beginning of loading.

195

196

Table 4. Parameters and results of push-out tests

Reference	Specimen	n_0	p (mm)	Studs	$0.5P_u$ (kN)	s_0 (mm)	K (kN/mm)
[8]	P-SB-1	8	200	M10 4.6	105	1.91	6.87
	P-SB-2	12	150	M10 4.6	150	1.73	7.23
	P-HSB-1	8	200	M10 8.8	170	2.26	9.40
	P-HSB-2	12	150	M10 8.8	200	1.69	9.86
[24]	Specimen 1	4	150	M10 6.8	47.9	2.13	5.70
	Specimen 2	4	150	M10 6.8	61.0	2.74	5.65
	Specimen 3	4	150	M10 6.8	61.4	2.31	6.67
	Specimen 4	4	150	M10 6.8	46.9	3.78	3.09
	Specimen 5	4	150	M10 6.8	55.3	2.54	5.53
[5]	SCS1	4	200	M8 8.8	40	0.92	10.87
	SCS2	4	200	M10 8.8	80	1.00	20.00
	SCS3	4	200	M10 8.8	60	1.25	12.00

197

198 4. Analytical Study on Shear Capacity

199 This section conducts analytical study on the shear behavior of FRP-concrete composite sections
200 considering slip effect and the distribution of shear stress in the FRP profile. Subsection 3.1 investigates the
201 interfacial slip behaviors. Subsection 3.2 investigates the shear stress distributions in FRP and concrete
202 considering the interfacial slip. Subsection 3.3 shows the validation of analytical results against the tests.

203 4.1. Interfacial slip

204 Similar to steel-concrete composite sections [28], an FRP-concrete composite section is composed of
205 an FRP profile and a concrete slab that are discontinuously connected, as shown in Fig. 8. Mechanical
206 analysis is conducted to analyze the FRP-concrete composite section based on the following assumptions:

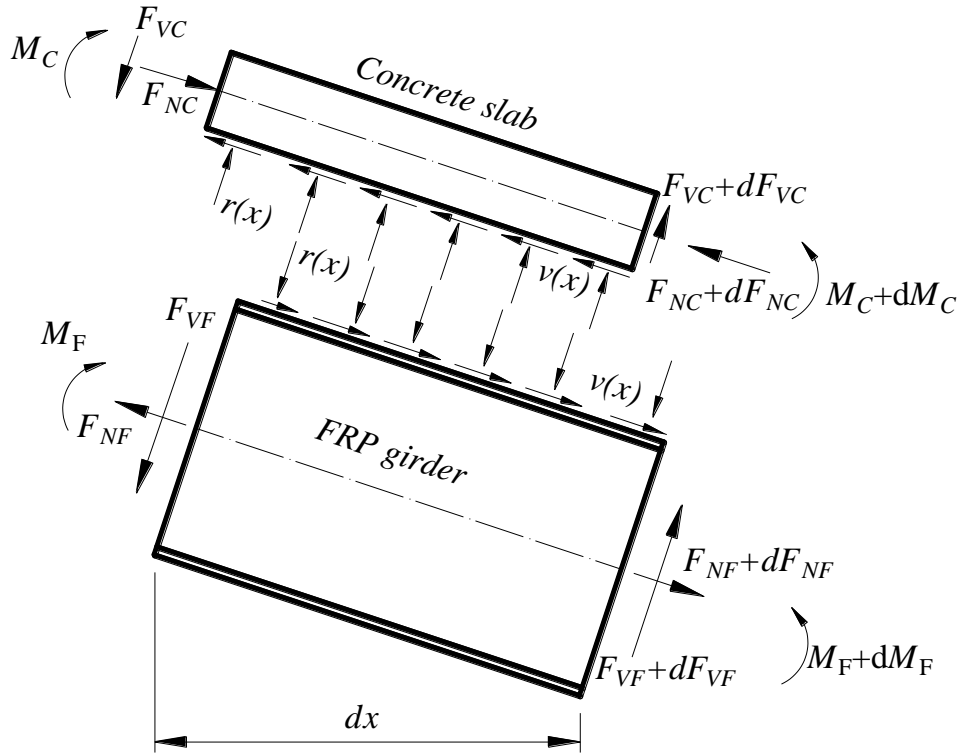
- 207 (i) Only the shear connectors and SIP formwork contribute to the shear connection between the FRP
208 and concrete. **The discrete connectors were smeared to the whole length of the interface, which is**
209 **similar to the analysis of steel-concrete composite sections [29][30][31]. By so doing, the model**
210 **does not distinguish between discontinuous and continuous layers connection.** For the specimens
211 with epoxy shear connection [32], FRP shear keys [8], and perforated FRP ribs [24], the interface
212 has full composite action, because the slip is very small compared with the specimens with steel
213 bolts.
- 214 (ii) The curvature and deflection of the FRP and concrete are the same. In other words, there is no
215 vertical separation (uplifting effect) at the interface, which has been the test results in Section 2.2.
- 216 (iii) Bernoulli's hypothesis on strain distribution is applicable to sections of FRP and concrete separately,
217 i.e., the shear deformation has been neglected, this may cause some error so the influence will be
218 discussed according to experimental test.

219 According to assumption (i), Eqs. (4) and (5) are obtained:

$$v(x) = ks(x) \tag{4}$$

$$k = nK/p \tag{5}$$

220 where $v(x)$ is the distributed interfacial shear force (see Fig. 8); x is the longitudinal coordinate with the
 221 origin at support point; k is the smeared slip modulus of the interface; $s(x)$ is the interfacial slip (see Fig.
 222 8); n is the number of rows of the connector in lateral direction; K is the slip modulus per connector defined
 223 by Eq. (3) from the push-out tests (see Fig. 7); p is the longitudinal space between two adjacent connectors.



224

Fig. 8. Model of sectional analysis of section dx .

225

226 According to equation of equilibrium of the infinitesimal (dx), in the horizontal (x) direction:

$$\frac{dN_C(x)}{dx} = \frac{dN_F(x)}{dx} = -v(x) \quad (6)$$

227

where $N_C(x)$ and $N_F(x)$ are the axial forces carried by concrete and FRP, respectively.

228

According to equation of equilibrium of the infinitesimal (dx), in the vertical (y) direction, the shear

229

force satisfies:

$$V_C(x) + V_F(x) = V(x) \quad (7)$$

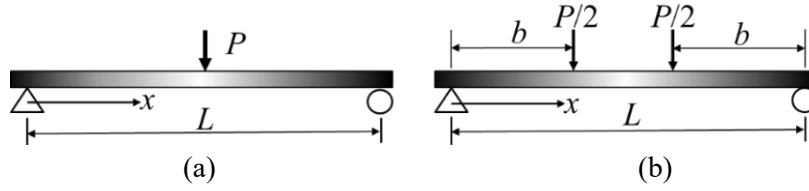
230

where $V_C(x)$ and $V_F(x)$ are the shear forces carried by the concrete and FRP, respectively; $V(x)$ is the total

231

shear force. Under three-point bending (Fig. 9a) or four-point bending (Fig. 9b): $V(x) = P/2$, where P is

232 the total applied load.



233
234 **Fig. 9.** Typical load definitions: (a) three-, and (b) four-point bending.

235 The moment equilibrium of the concrete and FRP segments gives:

$$\frac{dM_C(x)}{dx} - v(x) \frac{h_C}{2} + r(x) \frac{dx}{2} + V_C(x) = 0 \quad (8a)$$

$$\frac{dM_F(x)}{dx} - v(x) \frac{h_F}{2} - r(x) \frac{dx}{2} + V_F(x) = 0 \quad (8b)$$

236 where $M_C(x)$ and $M_F(x)$ are the moments carried by the concrete and FRP, respectively; h_C and h_F are the
237 depths of concrete and FRP, respectively (see Fig. 4a); $r(x)$ is the normal force along the FRP-concrete
238 interface.

239 According to assumption (ii), the curvature compatibility of the concrete and FRP gives:

$$\phi(x) = \frac{M_F(x)}{E_{Fx} I_F} = \frac{M_C(x)}{E_C I_C} \quad (9)$$

240 where E_{Fx} is the elastic modulus of FRP in x direction; I_F and I_C are the moment inertias of FRP and
241 concrete, respectively; E_C is the elastic modulus of concrete; $\phi(x)$ is the curvature of the beam.

242 For the constitutive relationships of the materials, linear elastic properties of the FRP and concrete are
243 adopted. The FRP is inherently linear elastic; the stresses in the concrete remain low before the FRP fails
244 with a shear failure, as supported by the test results in Section 2 and previous experiments in [8][11][21].
245 The longitudinal modulus of FRP is employed to compute the sectional rigidity, assuming the compressive
246 and tensile moduli of FRP are the same. Strains in the concrete $\varepsilon_C(x, y)$ and FRP $\varepsilon_F(x, y)$ are calculated
247 from the moment and axial force as:

$$\varepsilon_C(x, y) = \frac{M_C(x) \left(\frac{h_C}{2} - y \right)}{E_C I_C} - \frac{N_C(x)}{E_C A_C}, \quad 0 \leq y \leq h_C \quad (10a)$$

$$\varepsilon_F(x, y) = -\frac{M_F(x) \left(\frac{h_F}{2} + y \right)}{E_{Fx} I_F} + \frac{N_F(x)}{E_{Fx} A_F}, -h_F \leq y \leq 0 \quad (10b)$$

248 where A_C and A_F are the cross sectional areas of the concrete and FRP, respectively; y is vertical coordinate.

249 Eq. (11) gives the strains in the concrete and FRP at the interface.

$$\varepsilon_C(x, 0) = \frac{M_C(x) h_C}{2E_C I_C} - \frac{N_C(x)}{E_C A_C} \quad (11a)$$

$$\varepsilon_F(x, 0) = -\frac{M_F(x) h_F}{2E_{Fx} I_F} + \frac{N_F(x)}{E_{Fx} A_F} \quad (11b)$$

250 The strain difference caused by the slip at the interface, denoted as $\varepsilon_{slip}(x)$, is calculated as:

$$\varepsilon_{slip}(x) = \varepsilon_C(x, 0) - \varepsilon_F(x, 0) \quad (12)$$

251 The strain difference is equal to the first order derivation of the relative slip at the interface:

$$s'(x) = \varepsilon_{slip}(x) \quad (13)$$

252 Substituting Eqs. (8), (9), (11), and (12) into (13),

$$s'(x) = \phi(x) h_0 - \frac{N_C(x)}{E_C A_C} - \frac{N_F(x)}{E_{Fx} A_F} \quad (14)$$

253 where h_0 is the distance between the neutral axis of concrete and FRP, given by $h_0 = \frac{h_C + h_F}{2}$.

254 Solving Eqs. (6) and (14) yields:

$$\phi'(x) = \frac{V(x) - h_0 k s(x)}{E_{Fx} I_0} = \frac{V(x)}{E_{Fx} I_0} [1 - m(x)] \quad (15)$$

255 where $I_0 = I_C/\alpha_E + I_F$, $\alpha_E = E_{Fx}/E_C$, and $m(x) = h_0 k s(x)/V(x)$.

256 At the supports ($x = 0, L$), $m(x) = m_0$, where m_0 is a dimensionless factor depending on the shear
257 connection. The physical meaning of m_0 will be discussed in Section 4. Table 5 shows the solutions of m_0 .

258 Plugging Eq. (14) in Eq. (15), the governing equation of the relative slip is obtained:

$$s''(x) - \alpha^2 s(x) = -\alpha^2 \beta V(x) \quad (16)$$

259 where $\alpha = \sqrt{k A_1 / (E_{Fx} I_0)}$, $\beta = h_0 / k A_1$, $A_1 = I_0 / A_0 + h_0^2$, and $A_0 = A_F A_C / (\alpha_E A_F + A_C)$.

260 To solve Eq. (16), the boundary conditions are considered: $s(L/2) = 0$, and $\frac{ds(0)}{dx} = \frac{ds(L)}{dx} = 0$. Table

261 5 shows the solutions of interfacial slip under the three-point and four-point bending tests.

262 **Table 5.** Loads and corresponding solutions

Loads	Solution of $s(x)$	m_0	$m_{0,full}$
Fig. 9a	$\frac{\beta P}{2} \left[1 - \cosh(\alpha x) / \cosh\left(\frac{\alpha L}{2}\right) \right], 0 < x < L/2$	$\frac{h_0^2}{A_1} \left[1 - \operatorname{sech}\left(\frac{\alpha L}{2}\right) \right]$	$\frac{h_0^2}{A_1}$
Fig. 9b	$\begin{cases} \frac{\beta P}{2} \left\{ 1 - \operatorname{sech}\left(\frac{\alpha L}{2}\right) \cosh\left[\alpha\left(\frac{L}{2} - b\right)\right] \cosh(\alpha x) \right\}, 0 < x < b \\ \frac{\beta P}{2} \operatorname{sech}\left(\frac{\alpha L}{2}\right) \sinh\left[\alpha\left(\frac{L}{2} - x\right)\right] \sinh(\alpha b), b < x < L/2 \end{cases}$	$\frac{h_0^2}{A_1} \left[1 - \operatorname{sech}\left(\frac{\alpha L}{2}\right) \cosh\left[\alpha\left(\frac{L}{2} - b\right)\right] \right]$	$\frac{h_0^2}{A_1}$

263

264 4.2. Shear stress distributions in FRP and concrete

265 Fig. 10 shows the normal stress distribution in the FRP-concrete composite section. According to
 266 equation of equilibrium of the infinitesimal (dx) in x direction, Eq. (17) is obtained:

$$\tau_F(x, y)t(y)dx + \int_{-h_F}^y \sigma_F(x, y)t(y)dy = \int_{-h_F}^y \left[\sigma_F(x, y) + \frac{\partial \sigma_F(x, y)}{\partial x} dx \right] \cdot t(y)dy \quad (17)$$

267 where $\tau_F(x, y)$ is the shear stress of FRP; $t(y)$ is the thickness of FRP web or FRP width; $\sigma_F(x, y)$ is the
 268 normal stress of FRP.

269 Simplifying Eq. (17) and cancelling out the same items yield:

$$\tau_F(x, y)t(y) = \int_{-h_F}^y \frac{\partial \sigma_F(x, y)}{\partial x} t(y)dy \quad (18)$$

270 According to the Hook's law, the stress in the FRP can be expressed as:

$$\sigma_F(x, y) = E_{Fx} \varepsilon_F(x, y) \quad (19)$$

271 Substituting Eqs. (10a) and (19) to Eq. (18) yields:

$$\tau_F(x, y) = [V(x) - h_0 k s(x)] \frac{S_F(y)}{I_0 t(y)} + \frac{k s(x)}{t(y)} \cdot \frac{A_F(y)}{A_F}, -h_F \leq y \leq 0 \quad (20)$$

272 where $S_F(y) = \int_{-h_F}^y \left(y + \frac{h_F}{2} \right) t(y)dy$ and $A_F(y) = \int_{-h_F}^y t(y)dy$.

273 Analogously, the shear stress of concrete is written as:

$$\tau_C(x, y) = [V(x) - h_0 k s(x)] \frac{S_C(y)}{\alpha_E I_0 b_C} + \frac{k s(x)}{b_C} \cdot \frac{h_C - y}{h_C}, -h_F \leq y \leq 0 \quad (21)$$

274 where $\tau_C(x, y)$ is the shear stress of concrete, and $S_C(y) = \int_y^{h_C} b_C \left(y - \frac{h_C}{2} \right) dy$.

275 Eq. (20) can be used to obtain the shear stress of FRP web ($-h_F + t_{Flange} \leq y \leq -t_{Flange}$), where
 276 t_{Flange} is the thickness of FRP flange:

$$\tau_{F,web}(x, y) = \frac{V(x)}{t_{web}} \left[[1 - m(x)] \frac{S_F(y)}{I_0} + m(x) \frac{A_F(y)}{h_0 A_F} \right] \quad (22)$$

277 The maximum shear stress occurred symmetrically at two supports ($x = 0, L$), thus,

$$\tau_{F,web}(0, y) = \frac{P}{2t_{web}} \left[(1 - m_0) \frac{S_F(y)}{I_0} + m_0 \frac{A_F(y)}{h_0 A_F} \right] \quad (23)$$

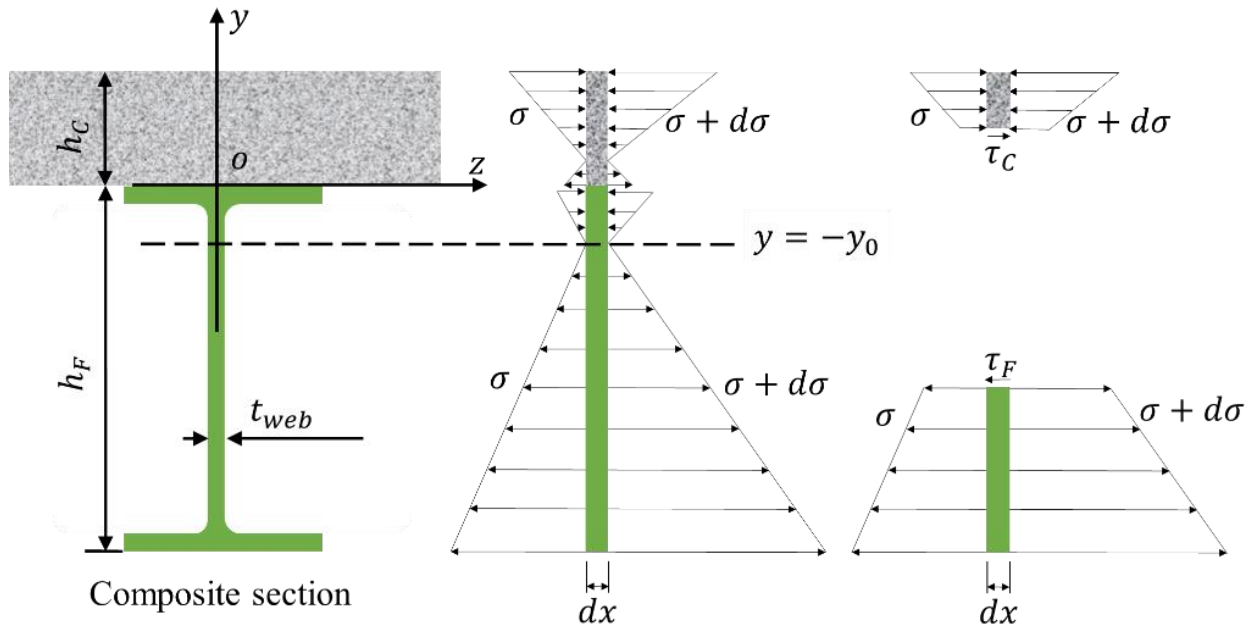
278 To locate the maximum shear stress, it is enforced that:

$$\frac{\partial \tau_{F,web}(0, y)}{\partial y} = 0 \quad (24)$$

279 Solving Eq. (24) gives the maximum shear stress (τ_{max}) at the point $(0, y_0)$, where y_0 is given by:

$$y_0 = \frac{I_0}{A_F h_0} \cdot \frac{1}{\frac{1}{m_0} - 1} - \frac{h_F}{2} \quad (25)$$

280 The analytical and experimental results of y_0 for the specimens in Section 2 are listed in Table 4. It
 281 can be deduced from the computation of y_0 that $-h_F/2 \leq y \leq -t_{Flange}$, meaning that the maximum shear
 282 stress (τ_{max}) is within the FRP web (Fig. 11a); $y \geq -t_{Flange}$, meaning that the maximum shear stress is
 283 within the FRP web-flange joint (Fig. 11b). Different failure criteria were used to predict the failure of FRP
 284 in past research. In this study, since the normal stress in the FRP web is far less than its strength, the
 285 maximum shear stress failure criterion is employed.



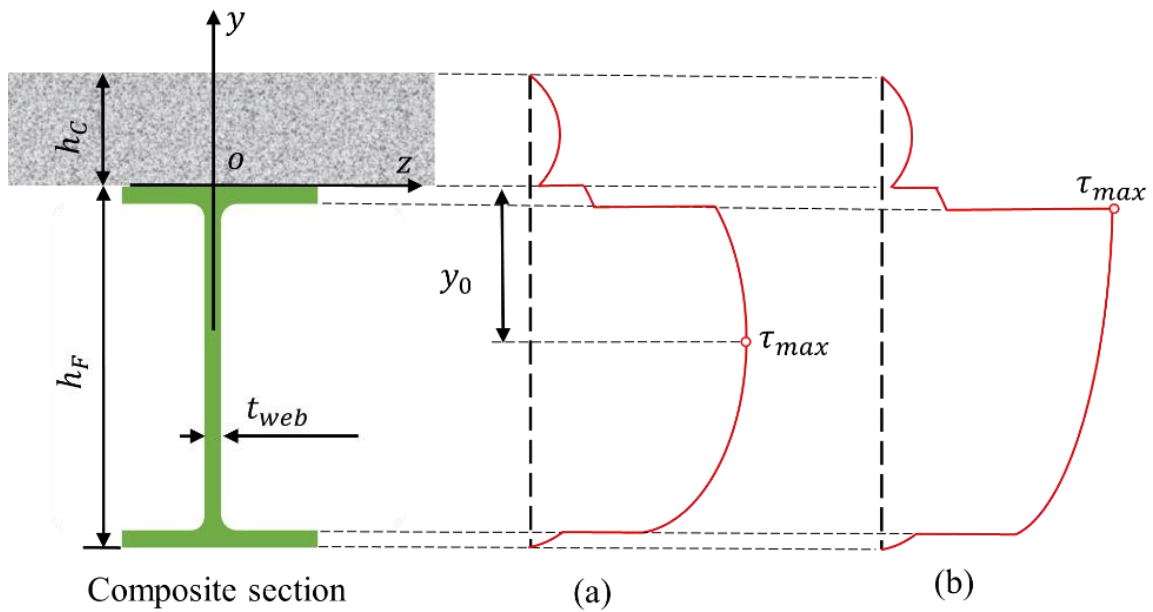
286

Composite section

287

Fig. 10. The distribution of the normal stress in the FRP-concrete composite section.

288



289

Composite section

(a)

(b)

290

Fig. 11. The maximum shear stress may occur in (a) the FRP web, and (b) the FRP web-flange joint.

291

4.3. Validation

292

Table 6 compares the shear strengths of specimens determined using the derived formulae and

293 experiments [5][12]. The average result of $\frac{\tau_{max}}{S_{xy}}$ is 1.023 with a coefficient of variation (CoV) of 0.162. The
 294 analytical results of y_0 are in Table 4, which shows good agreement with the measured values. The
 295 relatively high variation of $\frac{\tau_{max}}{S_{xy}}$ of the specimens in [5] is likely due to incorrect material strength data. For
 296 the rest of the specimens, $\frac{\tau_{max}}{S_{xy}}$ is close to 1.0, and CoV is small, revealing that Eq. (22) can be used to
 297 compute the shear stress. τ_{max} of specimen HB-T is 22% lower than S_{xy} , which is because the thick and
 298 wide concrete slab had some cracks when FRP failed. The influence of these cracks indicates that concrete
 299 damage should be considered when the concrete is thick compared with the depth of the FRP, which will
 300 be further researched.

301 Fig. 12 compares the shear strength of the FRP with the shear stress distribution along the depth of the
 302 FRP profile of each specimen listed in Table 6. In each specimen, the shear stress distribution is nonuniform
 303 and shows a parabolic shape. The shear stresses in the concrete are significantly lower than the shear stresses
 304 in the FRP profiles. This is associated with the larger thickness of the concrete.

305

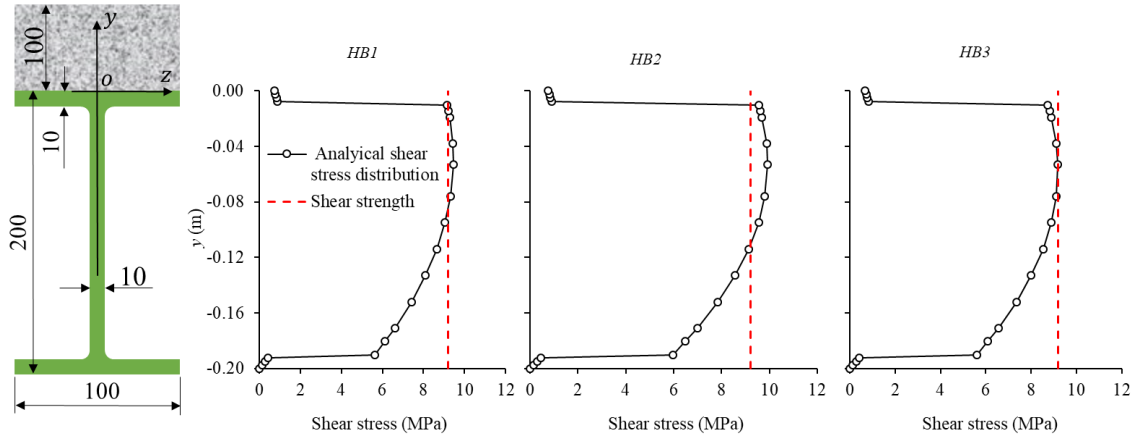
306 **Table 6.** Validation of shear stress in tested specimens with shear failure

Ref.	Specimen	$b_C \times h_C$ (mm×mm)	h_F (mm)	b_F (mm)	t_{Flange} (mm)	t_{web} (mm)	p (mm)	Push-out specimen	K (kN/mm)	L (m)	m_0	V_{test} (kN)	S_{xy} (MPa)	τ_{max} (MPa)	$\frac{\tau_{max}}{S_{xy}}$	η_F	η_{SD}
This study	HB-1	100×100	200	100	10	10	140	P-HSB [8]	9.63	2.6	0.597	18.7	9.2	9.43	1.025	0.85	1.15
	HB-2	100×100	200	100	10	10	170		9.63	2.6	0.582	19.5	9.2	9.93	1.079	0.86	1.10
	HB-3	100×100	200	100	10	10	220		9.63	2.6	0.558	17.9	9.2	9.20	1.000	0.87	1.18
[8]	HB	730×60	150	100	10	7	120	P-SB-SIP [8]	*a	2.1	0.538	49.6	25.3	28.30	1.119	0.59	1.29
	HB-T	730×110	150	100	10	7	120		*a	2.1	0.302	74.8	25.3	19.66	0.777	0.25	2.03
	HB-R	730×60	150	100	10	7	120		*a	2.1	0.538	47.3	25.3	27.19	1.075	0.59	1.35
[5]	HB1	400×100	120	60	10	10	130	SCS2 [5]	20	4.0	0.585	91.0	47.1	39.98	0.849	0.55	1.87
	HB3	400×100	120	60	10	10	130	SCS3 [5]	12	1.8	0.316	148.1	47.1	67.87	1.441	0.48	1.47
	HB5	400×100	120	60	10	10	130	SCS6 [5]	*b	1.8	0.592	87.9	47.1	38.62	0.820	0.55	2.01
[12]	M1-HB3	400×50	120	6	8	8	300	M6 [12]	5.78*c	1.8	0.329	81.1	35.0	33.62	0.961	0.63	1.31
	M1-HB4	400×50	120	6	8	8	300		5.78*c	1.8	0.329	85.6	35.0	35.48	1.014	0.63	1.24
	M2-HB3	400×50	120	6	8	8	300		5.78*c	1.8	0.336	89.8	35.0	37.21	1.063	0.63	1.19
	M2-HB4	400×50	120	6	8	8	300		5.78*c	1.8	0.329	91.3	35.0	37.84	1.081	0.63	1.16
Average															1.023	0.63	1.41
CoV															0.162	0.27	0.24

307 *a. Full composite action was employed in the specimens because SIP formwork was used and there was no slip at
 308 the interface in [8].

309 *b. Full composite action was ensured by using epoxy resin as connection SCS6 in [5].

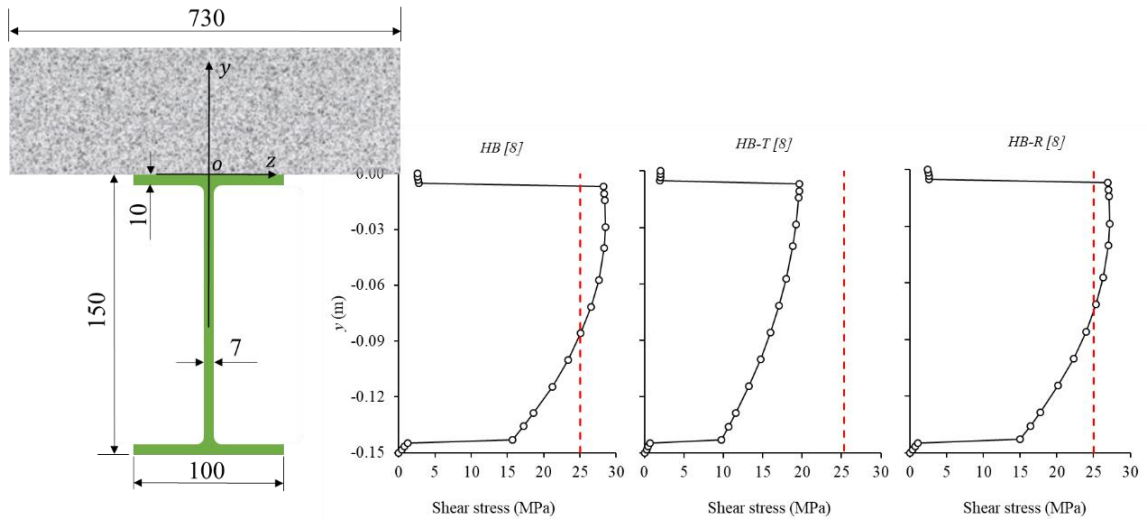
310 *c. The value of K was assumed as 80% of M10 stud, because of lack of push-out test data for the studs.



311

312

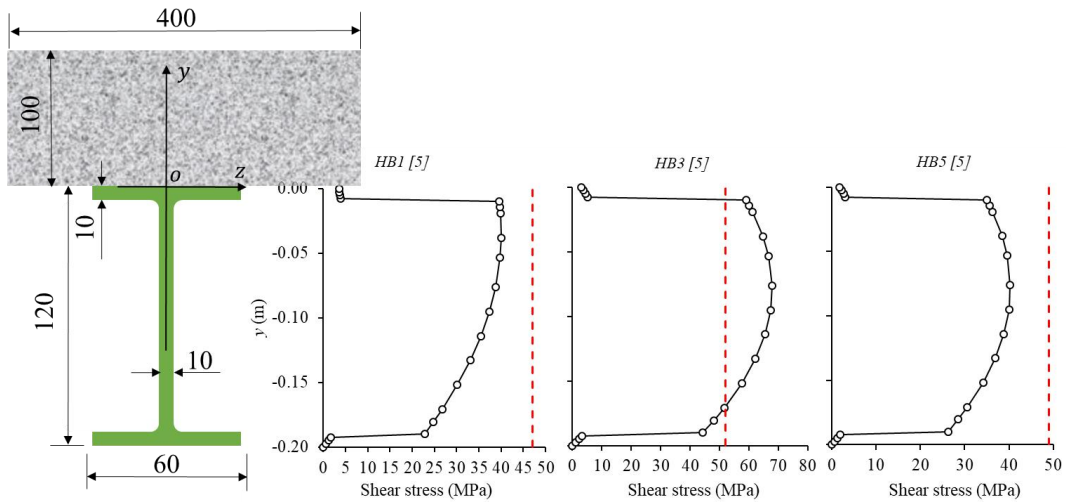
(a)



313

314

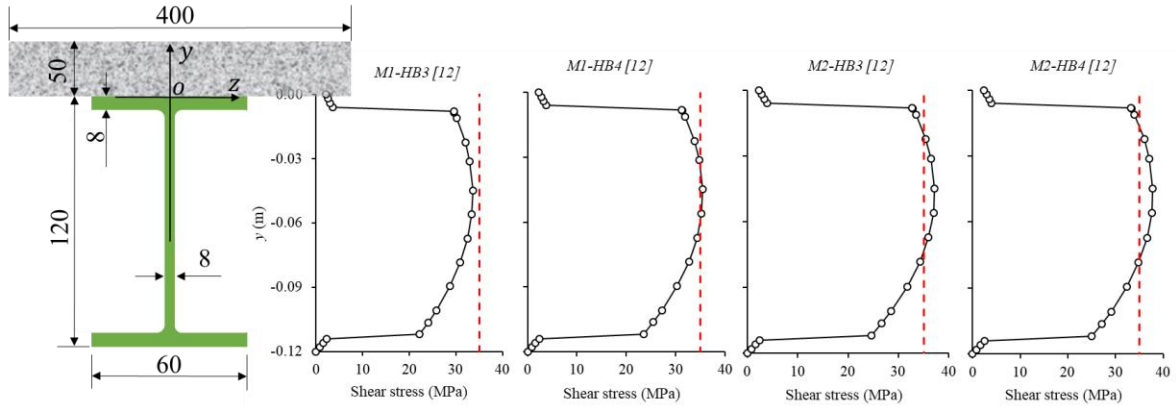
(b)



315

316

(c)



(d)

Fig. 12. Analytical shear stress distribution of FRP at failure load of specimens in: (a) the present study, (b) [8], (c) [5], and (d) [12]

5. Discussions

Based on the formulae derived in Section 3, parametric studies are performed to understand the effects of key parameters on the shear behavior and discuss the composite actions. The investigated parameters include the space of adjacent connectors, the thickness of FRP web, longitudinal modulus of FRP, and thickness of the concrete slab.

5.1. Parametric study

The geometry and materials in specimens HB1 to HB3 are used as the control in the parametric study for a FRP-concrete composite deck: $h_C = 100$ mm, $h_F = 200$ mm, $b_C = b_F = 100$ mm, $t_{Flange} = t_{web} = 10$ mm, $p = 200$ mm, $K = 8$ kN/mm, $L = 2.6$ m, $E_{Fx} = 12.8$ GPa, and $E_C = 29.5$ GPa.

Fig. 13 shows that as the space of adjacent connectors, p , increases from 0 to 5 m, m_0 decreases from 0.65 to 0.10. At $p = 0$, the FRP-concrete composite deck has full composite action, resulting in $m_0 = \frac{h_0^2}{A_1}$.

As p approaches to infinite, there is no composite action, and m_0 decreases to 0. Thus, it is rational to use the ratio of m_0 and $\frac{h_0^2}{A_1}$ to characterize the degree of composite action of the composite sections: full

composite action is represented by $\frac{m_0}{(h_0^2/A_1)} = 1.0$; non-composite action is represented by $\frac{m_0}{(h_0^2/A_1)} = 0$.

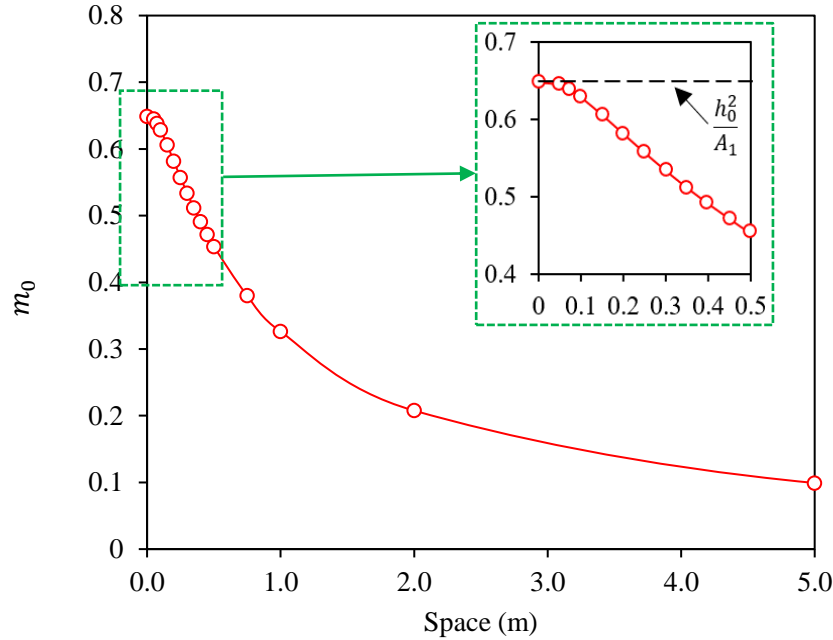


Fig. 13. The relationship between the space of connector and m_0 .

335

336

337

338

339

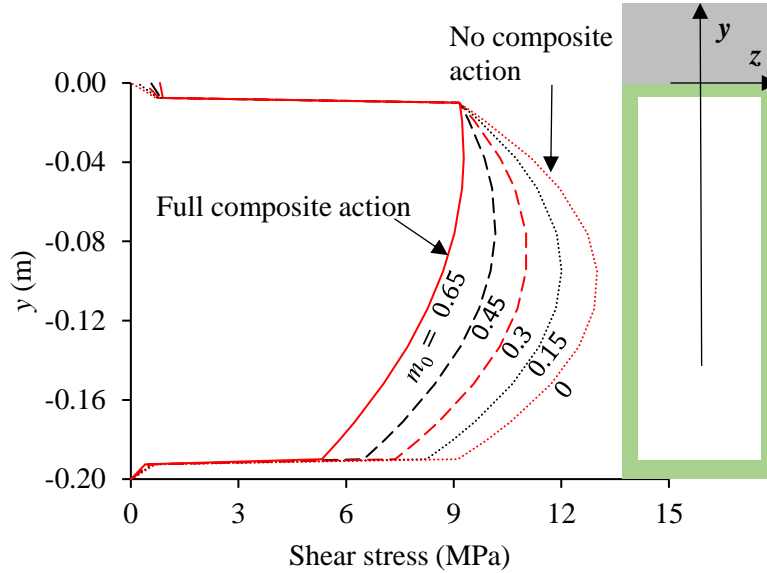
340

341

342

343

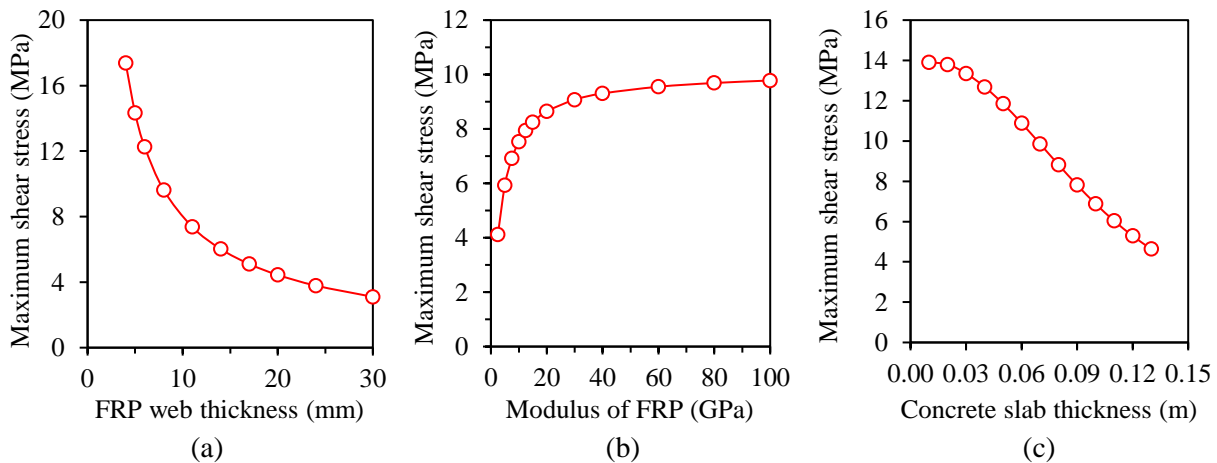
Fig. 14 shows that as m_0 increases from 0 to $h_0^2/A_1 (=0.65)$, the maximum shear stress decreases, and the neutral axis of the FRP moves from the center of the FRP web to the upper flange-web joint. For a beam with the same geometry and material properties, as the shear connection changes from non-composite action to full-composite action ($\frac{m_0}{(h_0^2/A_1)}$ increases from 0 to 1), the maximum shear stress decreases from 12.9 MPa to 9.4 MPa. Therefore, the shear connection plays a significant role in the shear capacity of the FRP-concrete composite sections.



344

345 **Fig. 14.** Effect of composite action degree on the shear stresses in FRP-concrete composite section.

346 Fig. 15 shows the effects of the thickness of FRP web, longitudinal modulus of FRP, and thickness of
 347 the concrete slab on the maximum shear stress. As the thickness of FRP web (t_{web}) increases from 4 mm
 348 to 30 mm, the maximum shear stress decreases from 17.4 MPa to 3.1 MPa (see Fig. 15a). As the longitudinal
 349 modulus of FRP (E_{Fx}) increases from 2.5 GPa to 100 GPa, τ_{max} increases from 4.1 MPa to 9.8 MPa (see
 350 Fig. 15b). As the thickness of the concrete slab (h_c) increases from 0.01 m to 0.13 m, the maximum shear
 351 stress decreases from 13.9 MPa to 4.6 MPa (see Fig. 15c).

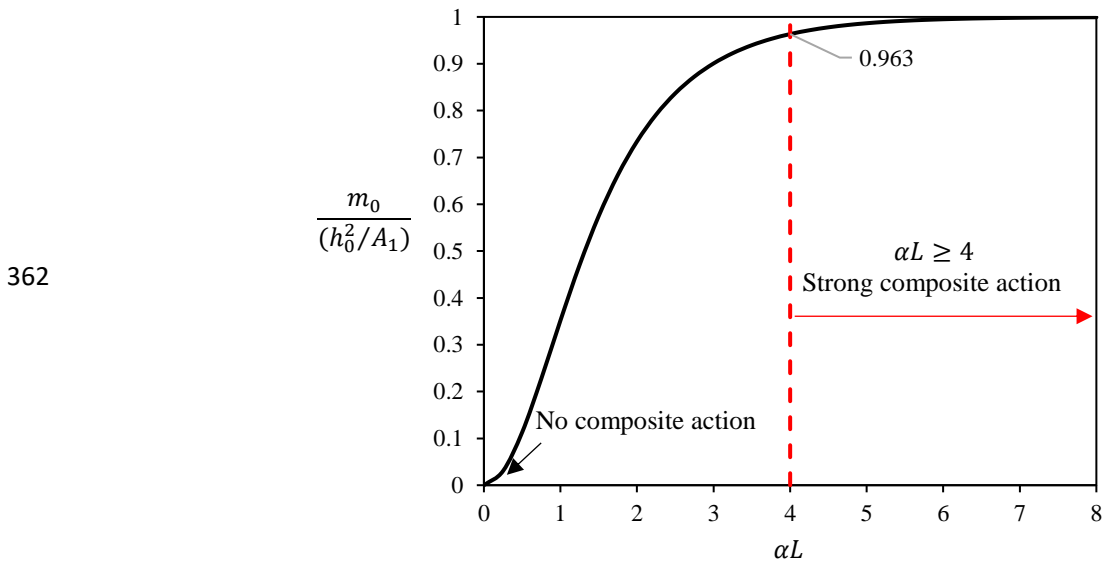


352

353 **Fig. 15.** Parametric study of the effect of (a) thickness of FRP web, (b) longitudinal modulus of FRP, and
 354 (c) height of concrete slab on the maximum shear stress.

355 **5.2. Composite action**

356 Fig. 16 plots the relationship between αL and $\frac{m_0}{(h_0^2/A_1)}$ under three-point bending. With $\alpha = 0$, it can be
 357 calculated that $m_0 = 0$ and $y_0 = -h_F/2$, which means the neural axis locates in the center of the FRP
 358 section. Previous tests showed that strong shear connections along the FRP-concrete interface were
 359 obtained using adhesive-studs mixed connection [5], FRP shear keys [32], or perforated FRP ribs [24]. With
 360 a high degree of composite action, $\alpha L \geq 4$, and $\frac{m_0}{(h_0^2/A_1)} \geq 0.963$. Since 0.963 is close to 1.0, the above
 361 equations can be reconstructed by replacing m_0 with $m_{0,full}$ (see Table 5) when $\alpha L \geq 4$.



363 **Fig. 16.** The influence of the degree of composite action.

364 **6. Design Method**

365 At the supports, the shear forces carried by concrete and FRP are obtained by integrating the shear
 366 stress in the height (y) direction:

$$V_C = \int_0^{h_C} \tau_C(0, y_0) b_C dy = \frac{P}{2} \left[(1 - m_0) \frac{I_C / \alpha_E}{I_0} + m_0 \frac{h_C}{h_C + h_F} \right] \quad (26a)$$

$$V_F = \int_{-h_F}^0 \tau_F(0, y_0) t(y) dy = \frac{P}{2} \left[(1 - m_0) \frac{I_F}{I_0} + m_0 \frac{h_F}{h_C + h_F} \right] \quad (26b)$$

367 where b_C is the width of concrete. **It should be noted that the shear lag effect has been observed and**
 368 **analyzed in steel-concrete composite sections where wider concrete slabs were used and higher stress**

369 level were reached, so an effective width was used instead of the whole width of concrete [33][34][35].
 370 But in this study, effective width was not considered. Further studies about the shear lag effect of concrete
 371 slab and FRP flange can be conducted, and the effective width can be used to replace b_c here.

372 Rewriting Eq. (26) gives the contributions of concrete and FRP girder:

$$V_C = \frac{P}{2}\eta_C \quad (27a)$$

$$V_F = \frac{P}{2}\eta_F \quad (27b)$$

373 where, η_C and η_F denote the contribution ratios of concrete and FRP, respectively ($\eta_C + \eta_F=1$):

$$\eta_C = (1 - m_0) \frac{I_C/\alpha_E}{I_0} + m_0 \frac{h_C}{h_C + h_F} \quad (28a)$$

$$\eta_F = (1 - m_0) \frac{I_F}{I_0} + m_0 \frac{h_F}{h_C + h_F} \quad (28b)$$

374 Eqs. (27) and (28) indicate that the contributions of FRP and concrete depend on the degree of
 375 composite action (related to m_0) and the flexural rigidity ratio ($\frac{I_C/\alpha_E}{I_0}$ or $\frac{I_F}{I_0}$), assuming that the elastic
 376 modulus and height ratio ($\frac{h_C}{h_C+h_F}$ or $\frac{h_F}{h_C+h_F}$) are constant. It should be noted that when thicker and wider
 377 concrete slab was used, the concrete will crack under tensile stress, which may reduce the moment inertias
 378 of concrete, see I_C in Eqs. (9) and (23a). So more test data for wider and thicker concrete slab are needed
 379 to modify the shear capacity of concrete slab.

380 In I_F , the contribution of the FRP web can be neglected. Therefore, Eq. (27b) can be rewritten as:

$$\eta_F = (1 - m_0) \frac{1}{1 + \frac{b_c h_c^3}{24\alpha_E t_F b_F h_F^2}} + m_0 \frac{h_C}{H} = \frac{1 - m_0}{1 + \frac{1}{12\alpha_E \alpha_1 \alpha_2^2}} + \frac{m_0}{1 + \alpha_2} \quad (29)$$

381 where $\alpha_1 = \frac{2t_F b_F}{b_c h_c}$, which is the ratio of cross sectional area of FRP flanges over concrete; $\alpha_2 = \frac{h_F}{h_c}$, which
 382 is the ratio of height of FRP girder over concrete; η_F can be used to evaluate the composite action between
 383 FRP and concrete.

384 Eq. (29) shows that m_0 and α_2 are the two main parameters that determine the contribution of FRP on

385 the shear capacity. The value of η_F using Eq. (27b) has an average value of 0.63, as shown in Table 5. In
 386 this study, η_F is larger than 0.85, because the width of concrete is small; the average result of η_F is less than
 387 0.63 for the rest of specimens in [5][12], because the section of concrete is wide compared with the FRP.

388 The design equation can be given by modifying Eq. (1):

$$V = \frac{1}{\eta} A_{web} S_{xy} \quad (30)$$

389 Herein, rewriting Eq. (30) gives:

$$\eta = \frac{A_{web} S_{xy}}{V} \quad (31)$$

390 Considering the ultimate state $S_{xy} = \tau_{max}$, η is expressed as:

$$\eta = \frac{A_{web} \tau_{max}}{V} \quad (32)$$

391 Rewriting Eq. (32) gives:

$$\eta = \eta_F \frac{A_{web} \tau_{max}}{V_F} = \eta_F \frac{\tau_{max}}{\tau_{avg}} = \eta_F \eta_{SD} \quad (33)$$

392 where $\tau_{avg} = V_F/A_{web}$, which is the average shear stress of FRP web, and $\eta_{SD} = \tau_{max}/\tau_{avg}$ is the ratio
 393 of the maximum shear stress over the average shear stress.

394 It is interesting that Eq. (1) can be obtained from Eqs. (30) and (33) by enforcing: $\eta_F = 1.0$ and $\eta_{SD} = 1.0$.
 395 Similarly, Eq. (2) can be obtained by enforcing: $\eta_F = 1.0$ and $\eta_{SD} = 1.5$. Eqs. (30) and (33) show that there
 396 are two factors that affect the accuracy, which are the contribution of the concrete and the nonuniform
 397 distribution of shear stress along the FRP profile. η_F can be quantified using Eq. (27b) or approximately by
 398 Eq. (29). The value of η_{SD} mainly depends on the location of the neutral axis and the distribution of shear
 399 stress. In order to get a design value for η_{SD} , the beams in Table 5 are used to inversely calibrate η_{SD} . To
 400 be specific, the following equation can be used:

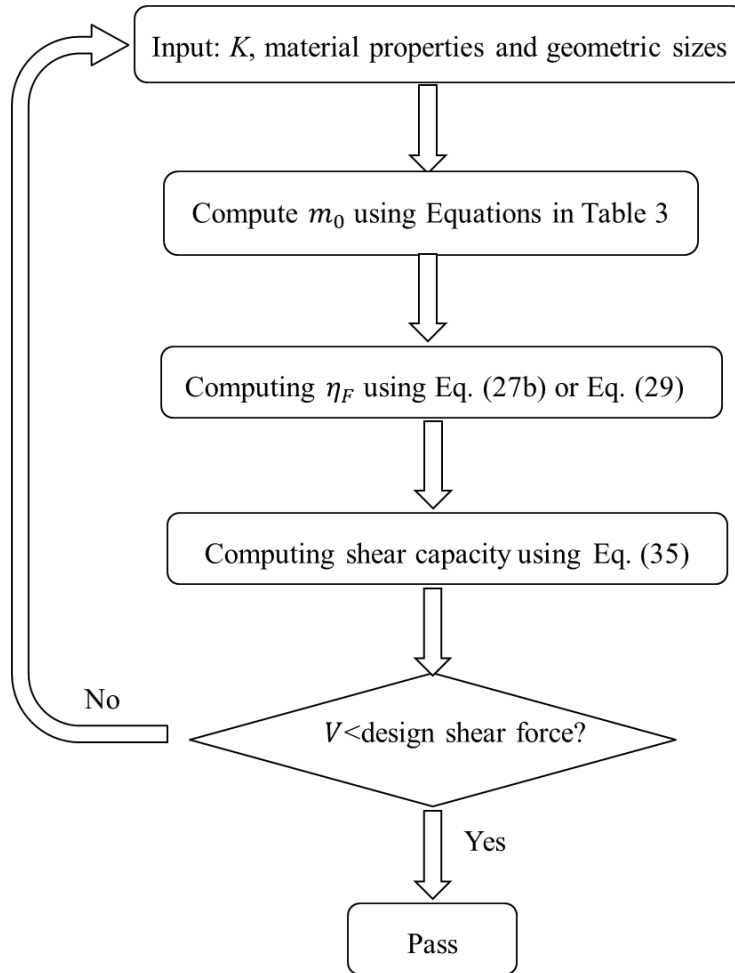
$$\eta_{SD} = \frac{\eta}{\eta_F} = \frac{A_{web} S_{xy}}{\eta_F V_{u.test}} \quad (34)$$

401 It can be seen that η_{SD} has an average value of 1.41, which is between 1.0 and 1.5 given by Eqs. (1)
 402 and (2), respectively. Herein, it is suggested that $\eta_{SD} = 1.41$ can be used for the design. Therefore, the final

403 design equation is given as:

$$V = \frac{1}{1.41\eta_F} A_{web} S_{xy} \quad (35)$$

404 However, since it remains unclear whether the value of 1.41 is suitable for all cases. Further research
405 is needed to obtain more test data to determine η_{SD} . The design procedure can be depicted using Fig. 17.



406

407 **Fig. 17.** The procedure to design an FRP-concrete composite section with adequate shear capacity.

408

409 7. Conclusions

410 This study investigates the shear behaviors of FRP-concrete composite sections by experiments and
411 analysis. Practical formulae were developed to predict the shear capacity of the composite sections. Based
412 on the above experimental and analytical investigations, the following conclusions are drawn:

- 413 (i) The shear failure mode of FRP-concrete composite sections is brittle and characterized by the
414 fracture along the horizontal direction at FRP webs or the upper web-flange joint.
- 415 (ii) When steel studs are used to connect the FRP and concrete, partial composite action is achieved,
416 which yields to an increase of shear stress compared with full composite action scenario.
- 417 (iii) The partial interaction between FRP and concrete is modeled by considering slip effect and
418 composite action degree that depends on the stiffness and spacing of the shear connectors. A
419 closed-form equation for shear capacity of the composite sections is derived based on the
420 maximum shear strength failure criterion of FRP webs.
- 421 (iv) The derived analytical equations can provide adequate predictions of the shear capacity and shear
422 stress distributions in the FRP-concrete composite sections. Based on the parametric analysis, a
423 simplified equation was derived for design.
- 424 (v) Parametric study shows that the shear capacity of the FRP-concrete composite sections is
425 significantly affected by the characteristics of the shear connectors (size, slip stiffness, and
426 spacing), the thickness of FRP web(s), and the thickness of concrete slab.

427 In the future, more tests are suggested to advance the understanding of the cracking of concrete slab
428 when wider and thicker concrete slab was used. Thus possible modification can be made on the parameter
429 η_F in the proposed design equation. Also, effective width can be used for concrete slab and FRP flange
430 when the shear lag effect is observed for larger or full-scale FRP-concrete hybrid sections.

431

432 8. Acknowledgments

433 The authors would like to thank the authors of reference [5] for providing the shear strength data of
434 their specimens. Thanks also go to Mr. Zhitao Chen and Mr. Songlin Li, formerly students advised by the
435 corresponding author, for their contribution to the tests.

436

437 9. Declaration of interests

438 Declarations of interest: none.

439 **10. Funding**

440 This work was supported by the National Natural Science Foundation of China (Grant No. 51678140).

441

442 **11. CRediT author statement**

443 **Xingxing Zou:** Conceptualization, Methodology, Experimental test, Writing- Original draft
444 preparation. **Peng Feng:** Supervision, Methodology, Funding acquisition. **Yi Bao:** Methodology, Writing-
445 Reviewing and Editing. **Jingquan Wang:** Supervision, Funding acquisition, Laboratory work support,
446 **Haohui Xin:** Writing- Reviewing.

447

448 **12. Data availability**

449 The raw data required to reproduce these findings cannot be shared at this time as the data is a part of
450 the ongoing funded project.

451

452 **13. References**

- 453 [1] Hollaway, L. C. (2010). A review of the present and future utilisation of FRP composites in the civil
454 infrastructure with reference to their important in-service properties. *Construction and building materials*,
455 24(12), 2419-2445.
- 456 [2] Kong, S. Y., Yang, X., and Lee, Z. Y. (2018). Mechanical performance and numerical simulation of
457 GFRP-concrete composite panel with circular hollow connectors and epoxy adhesion. *Construction and*
458 *Building Materials*, 184, 643-654.
- 459 [3] Nguyen, H., Mutsuyoshi, H., and Zatar, W. (2015). Hybrid FRP-UHPFRC composite girders: Part 1–
460 Experimental and numerical approach. *Composite Structures*, 125, 631-652.
- 461 [4] Gutiérrez, E., Primi, S., Mieres, J. M., and Calvo, I. (2008). Structural testing of a vehicular carbon fiber
462 bridge: Quasi-static and short-term behavior. *Journal of Bridge Engineering*, 13(3), 271-281.
- 463 [5] Correia, J. R., Branco, F. A., and Ferreira, J. (2009). GFRP-concrete hybrid cross-sections for floors of
464 buildings. *Engineering Structures*, 31(6), 1331-1343.

- 465 [6] Keller, T. (2001). Recent all-composite and hybrid fibre-reinforced polymer bridges and buildings.
466 Progress in Structural Engineering and Materials, 3(2), 132-140.
- 467 [7] Seible, F., Karbhari, V. M., and Burgueño, R. (1999). Kings stormwater channel and I-5/Gilman bridges,
468 USA. Structural Engineering International, 9(4), 250-253.
- 469 [8] Zou, X., Feng, P., Wang, J., Wu, Y., and Feng, Y. (2018). FRP stay-in-place form and shear key
470 connection for FRP-concrete hybrid beams/decks. Composite Structures, 192, 489-499.
- 471 [9] Ulloa, F. V., Medlock, R. D., Ziehl, P. H., and Fowler, T. J. (2004). Hybrid bridges in Texas. Concrete
472 international, 26(5), 38-43.
- 473 [10] Keller, T., Schaumann, E., and Vallée, T. (2007). Flexural behavior of a hybrid FRP and lightweight
474 concrete sandwich bridge deck. Composites Part A: Applied Science and Manufacturing, 38(3), 879-
475 889.
- 476 [11] Siwowski, T., Kaleta, D., and Rajchel, M. (2018). Structural behaviour of an all-composite road bridge.
477 Composite Structures, 192, 555-567.
- 478 [12] Neagoe, C. A., Gil, L., and Pérez, M. A. (2015). Experimental study of GFRP-concrete hybrid beams
479 with low degree of shear connection. Construction and Building Materials, 101, 141-151.
- 480 [13] Zhang, S., Xue, W. C., & Liao, X. (2019). Theoretical analysis on long-term deflection of GFRP-
481 concrete hybrid structures with partial interaction. Composite Structures, 216, 1-11.
- 482 [14] Sánchez-Aparicio, L. J., Ramos, L. F., Sena-Cruz, J., Barros, J. O., & Riveiro, B. (2015). Experimental
483 and numerical approaches for structural assessment in new footbridge designs (SFRSCC–GFPR hybrid
484 structure). Composite Structures, 134, 95-105.
- 485 [15] Chakraborty, A., Khennane, A., Kayali, O., & Morozov, E. (2011). Performance of outside filament-
486 wound hybrid FRP-concrete beams. Composites Part B: Engineering, 42(4), 907-915.
- 487 [16] Fiberline. 2002. Design manual, Kolding, Denmark.
- 488 [17] Strongwell. 2007. Design manual, Strongwell Corporation, Bristol, Va.
- 489 [18] Top Glass. 2008. "Technical data." <http://www.topglass.it/>.
- 490 [19] Creative Pultrusions. 2008. "Technical data." <http://www.creativepultrusions.com/>

- 491 [20] Meier, U., Triantafillou, T. C., and Deskovic, N. (1995). Innovative design of FRP combined with
492 concrete: short-term behaviour. *Journal of Structural Engineering*, 121(7), 1069-78.
- 493 [21] El-Hacha, R., and Chen, D. (2012). Behaviour of hybrid FRP-UHPC beams subjected to static flexural
494 loading. *Composites Part B: Engineering*, 43(2), 582-593.
- 495 [22] Iskander, M., El-Hacha, R., and Shrive, N. (2018). Governing failure criterion of short-span hybrid FRP-
496 UHPC beams subjected to high shear forces. *Composite Structures*, 185, 123-131.
- 497 [23] Zou, X., Feng, P., and Wang, J. (2018). Bolted shear connection of FRP-concrete hybrid beams. *Journal*
498 *of Composites for Construction*, 22(3), 04018012.
- 499 [24] Zou, X., Feng, P., and Wang, J. (2016). Perforated FRP ribs for shear connecting of FRP-concrete hybrid
500 beams/decks. *Composite Structures*, 152, 267-276.
- 501 [25] Nanjing Kangte Composite Material. <http://www.ktc-fiberglass.com/> (accessed in Dec. 2019)
- 502 [26] GB 50608–2010. Technical Code for Infrastructure Application of FRP Composites. China Architecture
503 & Building Press: Beijing, China, 2011. (in Chinese).
- 504 [27] GB 50010-2010. Code for Design of Concrete Structures. China Building Industry Press, Beijing, China,
505 2011 (in Chinese).
- 506 [28] Nie, J., and Cai, C. S. (2003). Steel–concrete composite beams considering shear slip effects. *Journal of*
507 *Structural Engineering*, 129(4), 495-506.
- 508 [29] Schnabl, S., Saje, M., Turk, G., and Planinc, I. (2007). Analytical solution of two-layer beam taking into
509 account interlayer slip and shear deformation. *Journal of Structural Engineering*, 133(6), 886-894.
- 510 [30] Johnson, R. P., Molenstra, N., & EPIB. (1991). Partial shear connection in composite beams for
511 buildings. *Proceedings of the Institution of Civil Engineers*, 91(4), 679-704.
- 512 [31] Wang, S., Tong, G., and Zhang, L. (2017). Reduced stiffness of composite beams considering slip and
513 shear deformation of steel. *Journal of Constructional Steel Research*, 131, 19-29.
- 514 [32] Alachek, I., Reboul, N., and Jurkiewicz, B. (2019). Experimental and finite element analysis of the long-
515 term behaviour of GFRP-concrete hybrid beams fabricated using adhesive bonding. *Composite*
516 *Structures*, 207, 148-165.

- 517 [33] Chen, Y., Dong, J., Xu, T., Xiao, Y., Jiang, R., and Nie, X. (2019). The shear-lag effect of composite box
518 girder bridges with corrugated steel webs and trusses. *Engineering Structures*, 181, 617-628.
- 519 [34] Amadio, C., Fedrigo, C., Fragiaco, M., and Macorini, L. (2004). Experimental evaluation of effective
520 width in steel–concrete composite beams. *Journal of Constructional Steel Research*, 60(2), 199-220.
- 521 [35] Zhu, L., and Su, R. K. L. (2017). Analytical solutions for composite beams with slip, shear-lag and time-
522 dependent effects. *Engineering Structures*, 152, 559-578.